scientific reports

Check for updates

OPEN

Hydrothermal synthesis of hierarchical microstructure tungsten oxide/carbon nanocomposite for supercapacitor application

Shanna Marie M. Alonzo[1], John Bentley[1], Salil Desai[2,3] & Bishnu Prasad Bastakoti[1,3]✉

A hierarchical nanocomposite of carbon microspheres decorated with tungsten oxide (WO_3) nanocrystals resulted from the hydrothermal treatment of a precursor solution containing glucose and tungstic acid. The dehydration of glucose molecules formed oligosaccharides, which consequently carbonized, turning into carbon microspheres. The carbon microspheres then acted as a spherical nucleus onto which WO_3 nanocrystals grew via heterogeneous nucleation. The reaction product showed a phase junction of orthorhombic and monoclinic WO_3, which transitioned to mix-phase of tetragonal and monoclinic WO_3 after a subsequent heat treatment at 600 °C in an inert condition. The electrochemical tests showed that incorporating WO_3 onto the carbon (WO_3/C) resulted in a three-fold increase in the specific capacitance compared to WO_3 alone and a high coulombic and energy efficiencies of 98.2% and 92.8%, respectively. The nanocomposite exhibited supercapacitance with both Faradaic and non-Faradaic charge storage mechanisms. Electrochemical impedance spectroscopy showed a lower charge transfer resistance for the composite at $R_{ct} = 11.7\Omega$.

Supercapacitors are widely recognized to fall into two categories based on their energy storage principle: electric double-layer capacitors (EDLC) and pseudocapacitors. In EDLC, when voltage is applied, ions from the electrolyte are attracted to the surface of the electrode, forming a double layer of charges and resulting in purely physical energy storage[1]. Carbon materials are often employed for EDLCs because of their high surface area, suitable pore size, good electrical conductivity, chemical stability, and versatility[2–4]. These properties, particularly the high surface area and chemical stability, aid in effective ionic physisorption during electrochemical processes. However, their drawback lies in their low specific capacitance and energy density[5]. Conversely, pseudocapacitors achieve energy storage through reversible oxidation–reduction (Faradaic) reactions at/near the electrode surface. The additional contribution from these chemical redox reactions during charge/discharge leads to a higher specific capacitance[6–8]. Among the various redox-active materials, transition metal oxides have gained significant attention as electrode materials due to their multiple oxidation states, which allow for improved pseudocapacitance[5,6,9]. Tungsten oxide (WO_3), a transition metal oxide with multiple crystal phases, exhibits favorable attributes as a pseudocapacitor[10–12]. Not only can it undergo reversible redox reactions between W^{5+} and W^{6+} ions, but the inherent voids in its crystal structure facilitate the smooth diffusion of ions from the electrolyte[13]. However, their limitations include relatively poor conductivity in bulk form and the tendency to aggregate during the charge/discharge process even in their nanostructure form, as is typical of transition metals[14].

WO$_3$ and carbon-based composites have been explored to address the abovementioned constraints in recent years. Combining WO_3 and carbon materials creates a synergistic effect that complements each other's limitations, leading to better overall performance[15]. The hybrid presents a viable approach to enhance the electronic conductivity of WO_3, improve the capacitance of carbon by incorporating redox reactions, lessen the aggregation of WO_3 nanocrystals, and provide overall structural stability[9]. Most of these works involved nanotubes, nanowires, nanoplates, and nanosheets prepared in non-aqueous solutions or with expensive polymeric templates[16].

[1]Department of Chemistry, North Carolina A&T State University, 1601 E. Market St., Greensboro, NC 27411, USA. [2]Department of Industrial and System Engineering, North Carolina A&T State University, 1601 E. Market St., Greensboro, NC 27411, USA. [3]Center of Excellence in Product Design and Advanced Manufacturing, North Carolina A&T State University, 1601 E. Market St., Greensboro, NC 27411, USA. ✉email: bpbastakoti@ncat.edu

Nayak et al. utilized a solvothermal approach to synthesize a WO_3 nanowire–graphene sheet composite[17]. Xiong et al.[18] and Shi et al.[19] prepared hierarchical ordered porous WO_3–carbon using discarded biomass as a precursor, with the former using glue milling and carbonization-activation method and the latter via a solvothermal process. Di et al. also used a solvothermal technique to decorate carbon nanotubes with an array of WO_3 nanosheets[20].

This work synthesized carbon microspheres decorated with WO_3 nanocrystals via a facile hydrothermal method using glucose as the carbon source. The simple procedure resulted in a hierarchical micro/nanostructure that could facilitate and enhance electrochemical reactions[21]. The crystal phase transformation of WO_3 in the presence of glucose and its effect on the capacitive behavior of the WO_3/C electrode was also investigated. Electrochemical tests revealed that the WO_3/C nanocomposite provided more pathways for charge diffusion within its structure. These pathways appear to result from a cooperative interplay between the intricate nanocrystalline mixed phase WO_3 and the porous carbon microsphere.

Experimental section
Materials
Analytical/reagent grade tungstic (VI) acid (H_2WO_4, Alfa Aesar), D(+)-glucose (Acros Organics), Nafion® D-521 (Alfa Aesar), ethanol (VWR Chemicals), and potassium hydroxide (Sigma-Aldrich) were used without further purification.

Synthesis of the WO_3/C composite and preparation of working electrodes
The precursor solution consisted of 1 g H_2WO_4 (dissolved in 5 mL ethanol), 1 g glucose, and 75 mL distilled water. The solution was transferred to a Teflon-lined stainless-steel autoclave, sealed, and heated at 180 °C for 20 h. After cooling, the hydrothermal reaction product was washed with water and ethanol before drying at 60 °C. Scheme 1 shows a graphical illustration of the hydrothermal synthesis. Carbon microspheres would form due to dehydration and oligosaccharide formation. Supersaturation would then lead to nucleation and subsequent growth of WO_3 nanocrystals on these spheres via heterogeneous nucleation[14,22].

The dried as-prepared sample was calcined at 600 °C for 3 hours at a ramping rate of 3°C/min in a nitrogen environment. A control sample without glucose was also prepared for comparison. 5 mg of the calcined powder sample was ground and dispersed in 500 μL ethanol to make the working electrodes. Then, 50 μL of the binder Nafion® D-521 was added. After mixing and sonicating, 220 μL of the slurry was drop-cast on copper substrates with a working area of 1.0 cm^2 and dried at 60 °C for 12 h.

Characterization
The crystal structure of the nanocomposites was studied by X-ray diffraction (XRD) using a Rigaku MiniFlex 600 diffractometer equipped with a Cu K$_\alpha$ radiation source and a scintillation counter detector. Powder XRD patterns were recorded from 10° to 60° (0.02° step, 2°/min speed) at 40 kV and 15 mA. Fourier transform infrared (FTIR) spectra were recorded from 400–4000 cm^{-1} using a Shimadzu IRTracer-100 spectrophotometer with a DLATGS detector. The Raman and X-ray photoelectron spectra were collected using a Horiba XploRA Raman confocal microscope and an ESCALAB™ XI + X-ray photoelectron spectrometer, respectively. The morphology and elemental mapping of the samples were investigated using a JEOL JSM-IT800 Schottky field emission scanning electron microscope (FESEM). For surface area and porosity analysis, N_2 adsorption–desorption isotherms were measured at 77 K using Quantachrome NovaWin. The electrochemical measurements were performed using a CH Instruments workstation with a three-electrode configuration. Copper foil, Ag/AgCl, platinum wire, and the synthesized materials were used as the current collector, reference electrode, counter electrode, and working electrodes, respectively. The electrolyte used was 0.1 M potassium hydroxide. The electrochemical tests included
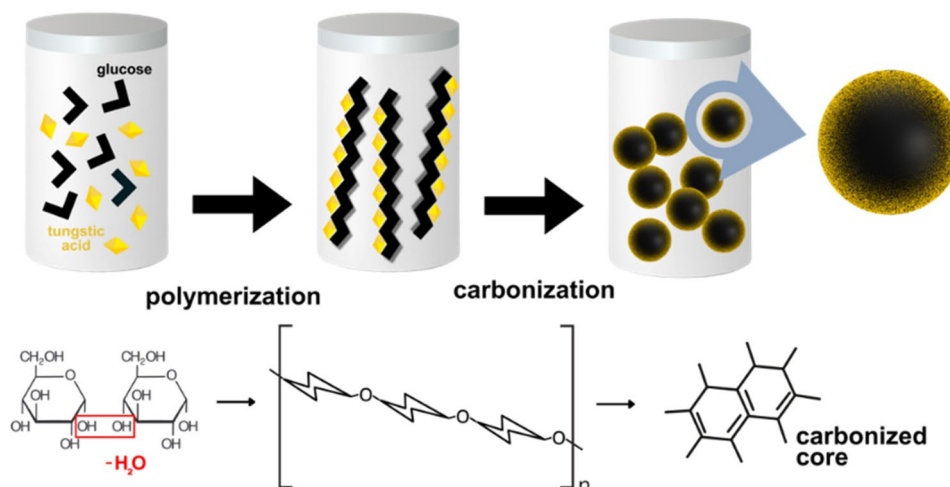
Scheme 1. Graphical illustration of the WO_3/C nanocomposite synthesis via a hydrothermal treatment strategy.

cyclic voltammetry (CV), galvanostatic charge–discharge (GCD), and impedance spectroscopy. The specific capacitance was calculated using Eq. (1), coulombic efficiency using Eq. (2), and energy efficiency using Eq. (3),

$$C_s = \frac{\int_{V_1}^{V_2} Idv}{2sm\Delta V}$$ (1)

$$\eta_c = \frac{t_d}{t_c} \times 100$$ (2)

$$\eta_E = \frac{E_{int/d}}{E_{int/c}} \times 100$$ (3)

where C_s is the specific capacitance (F/g), $\int_{V_1}^{V_2} Idv$ is the integral CV curve area (AV), s is the scan rate (V/s), m is the mass of the active material (g), ΔV is the potential window, η is the coulombic efficiency (%), t_d is discharging time (s), t_c is charging time (s), $E_{int/d}$ is the galvanostatic discharge energy, and $E_{int/c}$ is the galvanostatic charge energy[21,23,24].

Results and discussion

The samples' XRD patterns showed sharp and intensive peaks, indicating a crystalline structure. In Fig. 1A, the XRD pattern of the uncalcined WO$_3$/C composite (blue) is consistent with the orthorhombic crystal structure of WO$_3$ (JCPDS No. 43-0679) and diffractograms reported in the literature[25–27]. The strong peaks at 16.5° and 25.6° are attributed to the (020) and (111) reflections of the orthorhombic crystal structure of tungsten oxide hydrate (WO$_3$·H$_2$O), respectively. These peaks were not observed in the control sample WO$_3$ (Fig. 1A, red), which did not have glucose as a carbon precursor, suggesting that glucose aided in preserving the orthorhombic crystal-line phase of WO$_3$·H$_2$O during the hydrothermal process. The hydroxyl group in glucose and the hydrogen in the WO$_3$·H$_2$O molecule formed a hydrogen bond, promoting the controlled growth of WO$_3$·H$_2$O crystallites[28].

Moreover, the triplet peaks near 35.0° for the WO$_3$/C nanocomposite (Fig. 1A, blue) could be indexed to the orthorhombic (040), (200), and (002) crystal planes. But in the uncalcined WO$_3$ sample (Fig. 1A, red), these peaks appeared as a doublet at 34.1° and corresponded to the (202) plane, indicating a monoclinic structure[29–31]. The uncalcined nanocomposite WO$_3$/C showed a coexistence of orthorhombic and monoclinic phases, with the former as the dominant phase, and the control WO$_3$ exhibited a purely monoclinic phase. The sharp diffractive peaks at 23.1°, 23.7°, and 24.2° corresponded to the (002), (020), and (200) crystal planes, consistent with JCPDS No. 43–1035 for monoclinic WO$_3$. After calcination, as shown in Fig. 1B (red), the control WO$_3$ did not change its phase but exhibited increased crystallinity with peaks becoming sharper and more defined. For instance, the doublet peak at 34.1° diverged more clearly. The elevated temperature during calcination provided sufficient energy for adjacent tiny crystals to rearrange and coalesce into larger crystals[32,33]. This increase in crystallite size of WO$_3$ from 16 Å to 23 Å after calcination appeared as narrower, more intensified XRD peaks. On the other hand, the WO$_3$/C composite changed its phase after calcination (Fig. 1B, blue). The intense peaks at 16.5° and 25.6° characteristic of orthorhombic crystal, disappeared, indicating the removal of the hydrate water in WO$_3$·H$_2$O[25]. The XRD pattern after calcination showed a tetragonal/monoclinic phase junction. The main dif-fraction peaks at 23.0°, 23.9°, 28.7°, 33.5°, and 34.0° could be attributed to the (002), (110), (102), (112), and (200) planes of tetragonal WO$_3$, aligning with COD No. 1521532[34,35]. However, this attribution may not be absolute,
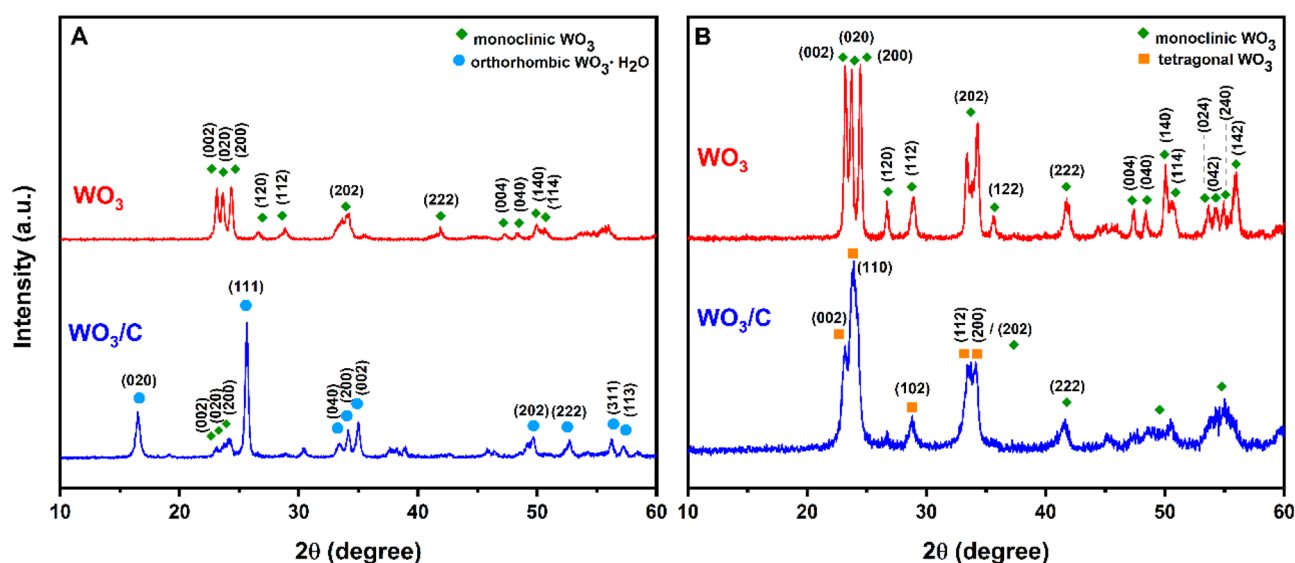

Figure 1. XRD patterns of WO$_3$ and WO$_3$/C (**A**) before calcination and (**B**) after calcination.

and a pseudo-phase consisting of orthorhombic and tetragonal phases would also be likely, as observed from previous work[13,34]. The less defined peaks from 45° to 60° resembled that of monoclinic WO_3 and indicated a reduced intensity due to the amorphous carbon. The energy storage performance of WO_3 depends on its crystal structure which influences the intercalation of ions in an electrochemical environment[5,9]. Orthorhombic and tetragonal WO_3 generally tend to have more cavities or open spaces within its crystal structure than monoclinic WO_3. The more open structure and wider tunnels in the former allow fast, reversible intercalation of ions[5,9,36].

The FTIR spectra (Fig. 2A) elucidated the different functional groups existing on the surface of the samples. For the uncalcined WO_3/C, the observed peak at 3387 cm^{-1} corresponded to the stretching vibrations of O–H from water molecules in $WO_3 \cdot H_2O$.

This peak was not as prominent in the uncalcined WO_3 sample, suggesting a significant elimination of crystalline water during the hydrothermal treatment, thereby corroborating with the XRD result. The 1616 cm^{-1} and 1704 cm^{-1} peaks confirmed carbon's presence in the nanocomposite. These spectral bands were associated with the vibrations of C=C and C=O, respectively, and supported the idea that glucose likely underwent aromatization during the hydrothermal treatment[22]. The peaks in the spectral range 500–1000 cm^{-1} were characteristic absorptions of tungsten oxide. The strong peak at about 600 cm^{-1} corresponded to the stretching vibrations of O–W–O. The stretching vibrations of W=O appeared as a sharp shoulder absorption peak at 802 cm^{-1} for the uncalcined and calcined WO_3 and for the calcined WO_3/C composite as well, although less sharp. Only the uncalcined WO_3/C showed a major characteristic band of the terminal oxygen atom (W=O) of the $WO_3 \cdot H_2O$ structure appearing at 937 cm^{-1}, again showing agreement with the XRD data[25,27,37].

The Raman scattering spectra of the calcined samples were also recorded. The spectrum for the control WO_3 sample exhibited two intense peaks at 701 cm^{-1} and 791 cm^{-1}, corresponding to the stretching vibration of tungsten atoms with neighboring oxygen atoms (O–W–O) as shown in (Fig. 2B). These peaks became less intense in the presence of carbon in the WO_3/C nanocomposite. The prominent peaks at 1334 cm^{-1} (D band) and 1577 cm^{-1} (G band) could be ascribed to the absorption of sp^3-hybridized carbon and sp^2-hybridized carbon, respectively. The D band is linked to structural disorder and defects, while the G band indicates the graphitization of carbon. Even though the XRD peaks for graphitic carbon ((002) at 24° and (100) at 43°) were overshadowed by the highly crystalline WO_3, the Raman spectrum for WO_3/C confirmed its presence. The intensity ratio of the D to the G peak (I_D/I_G) was measured at 0.818, attributing the higher G band to the graphitic clusters in the amorphous composite[3,25,38,39].

The nanocomposite morphology was observed by SEM (Fig. 3A,B) and TEM (Fig. 3C,D). Carbon spheres were derived from glucose during the hydrothermal treatment at 180 °C which is higher than the typical glycosylation temperature, resulting in aromatization and carbonization. Glucose molecules underwent dehydration and formed oligosaccharides, resembling a polymerization process. The new carbon–carbon bonds eventually formed the carbon microspheres of > 1.0 μm in diameter. It could be presumed that within the 20 h hydrothermal reaction, the solution reached a critical supersaturation, and a burst of nucleation ensued, crosslinking the previously formed oligosaccharides. This aggregation of glucose consequently acted as a spherical nucleus onto which WO_3 nanocrystals grew via heterogeneous nucleation[14,22]. This process successfully formed a nanocomposite consisting of tungsten oxide and carbon (WO_3/C), as confirmed by the elemental mapping of a single sphere by energy-dispersive x-ray (EDX) spectroscopy (Fig. 3B). The EDX mapping spectrum revealed 56.9% C, 37.2% W, and 5.9% O (Supporting Information Fig. S1). The SEM images of WO_3 synthesized without using glucose are shown in Fig. S2. Additionally, the lack of peaks in the range 1000 cm^{-1} to 1300 cm^{-1} in the FTIR spectrum of the uncalcined WO_3/C further supported the loading of WO_3 nanocrystals onto the carbon microspheres. Peaks
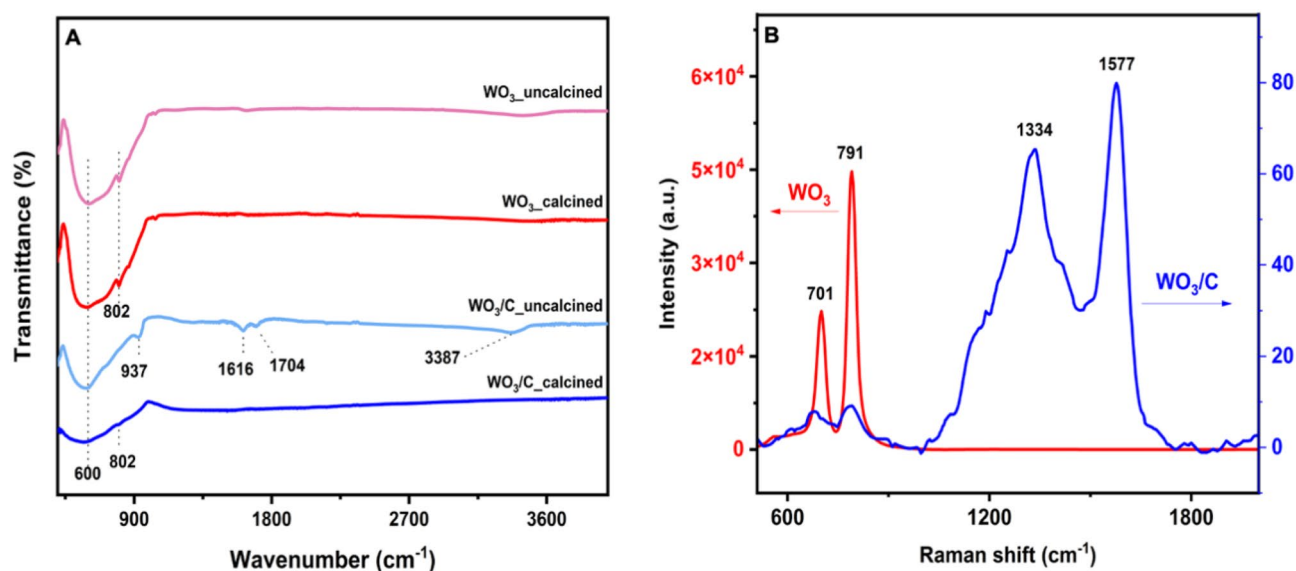

Figure 2. (**A**) FTIR spectra of the samples before and after calcination and (**B**) Raman spectra of calcined WO_3 and WO_3/C nanocomposite after calcination.
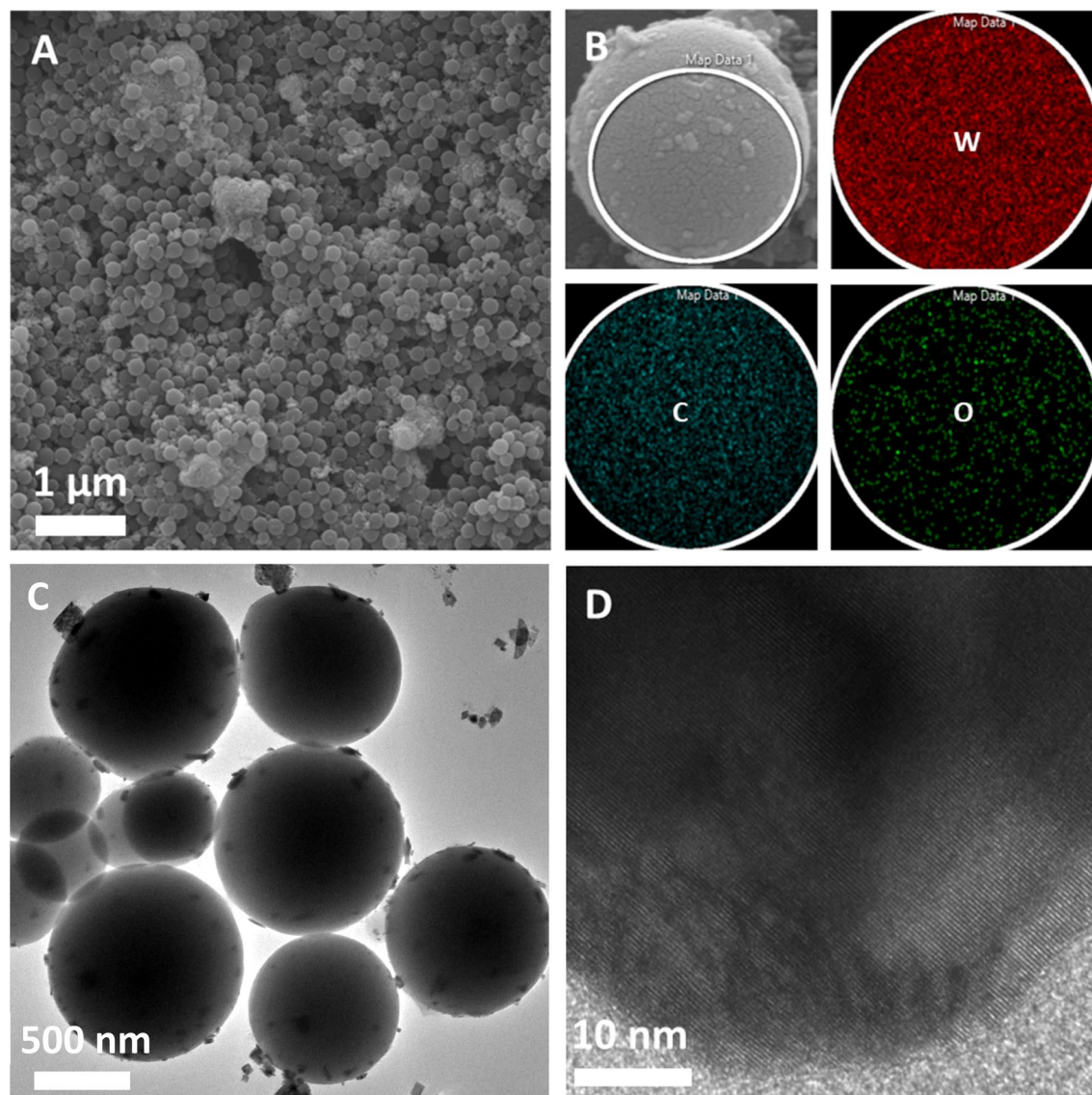
Figure 3. (**A**) Scanning electron microscopy (SEM) images of WO$_3$/C. (**B**) Elemental mapping of WO$_3$/C (red = W, teal = C; green = O) by energy-dispersive x-ray (EDX) spectroscopy. (**C**) TEM image WO$_3$/C and (**D**) HRTEM of WO$_3$ nanocrystal attached on carbon surface.

in this range would have indicated C–OH stretching and OH bending vibrations from residual hydroxy groups. The lack thereof suggested that the hydroxyl groups of glucose have formed hydrogen bonds with WO$_3$·H$_2$O, which preserved the orthorhombic structure of the latter, as previously discussed in the XRD findings.

Results from the elemental mapping by EDX of the WO$_3$/C nanocomposites were further confirmed by x-ray photoelectron spectroscopy (XPS). The XPS survey spectrum of the nanocomposite showed the presence of W, O, and C elements (Fig. S3). Furthermore, a comparison of the W 4f. spectra of the WO$_3$/C nanocomposite (Fig. 4A) with that of WO$_3$ (Fig. 4B) shows that introducing carbon in the nanocomposite altered the chemical state of tungsten. The WO$_3$/C nanocomposite exhibited three resolved peaks, whereas WO$_3$ alone displayed just a pair of peaks in the deconvoluted spectra. In the WO$_3$ spectrum, the peaks at 35.1 eV (W 4f$_{7/2}$) and 37.5 eV (W 4f$_{5/2}$) corresponded to the W^{6+} oxidation state[34,40,41]. These shifted to slightly higher binding energies in WO$_3$/C (36.2 eV and 39.6 eV), indicating a change in the chemical environment of tungsten. The nanocomposite also displayed peak broadening, particularly in W 4f$_{5/2}$ (FWHM of WO$_3$ = 2.3 eV; WO$_3$/C = 6.7 eV), further confirming alterations in the number of chemical bonds[42]. A third peak at 34.3 eV was also present in the nanocomposite and could be ascribed to W^{x+} (where $4 < x < 6$). A similar peak was also observed in another work wherein WO$_3$-carbon nanotubes showed tetragonal WO$_3$ in its XRD[43], similar to this work. They found that the existence of W^{x+} was beneficial for increasing conductivity and, thereby, electrochemical performance. It is also worth mentioning that the WO$_3$/C nanocomposite had higher-intensity W 4f. peaks than the pristine WO$_3$. This might be explained by the increase in the effective surface area of the nanocomposite since carbon materials often have higher surface areas than metal oxides. The more intense XPS signals could be due to the larger fraction of the surface being probed during the analysis. This higher intensity was also observed in the O 1s spectra of the
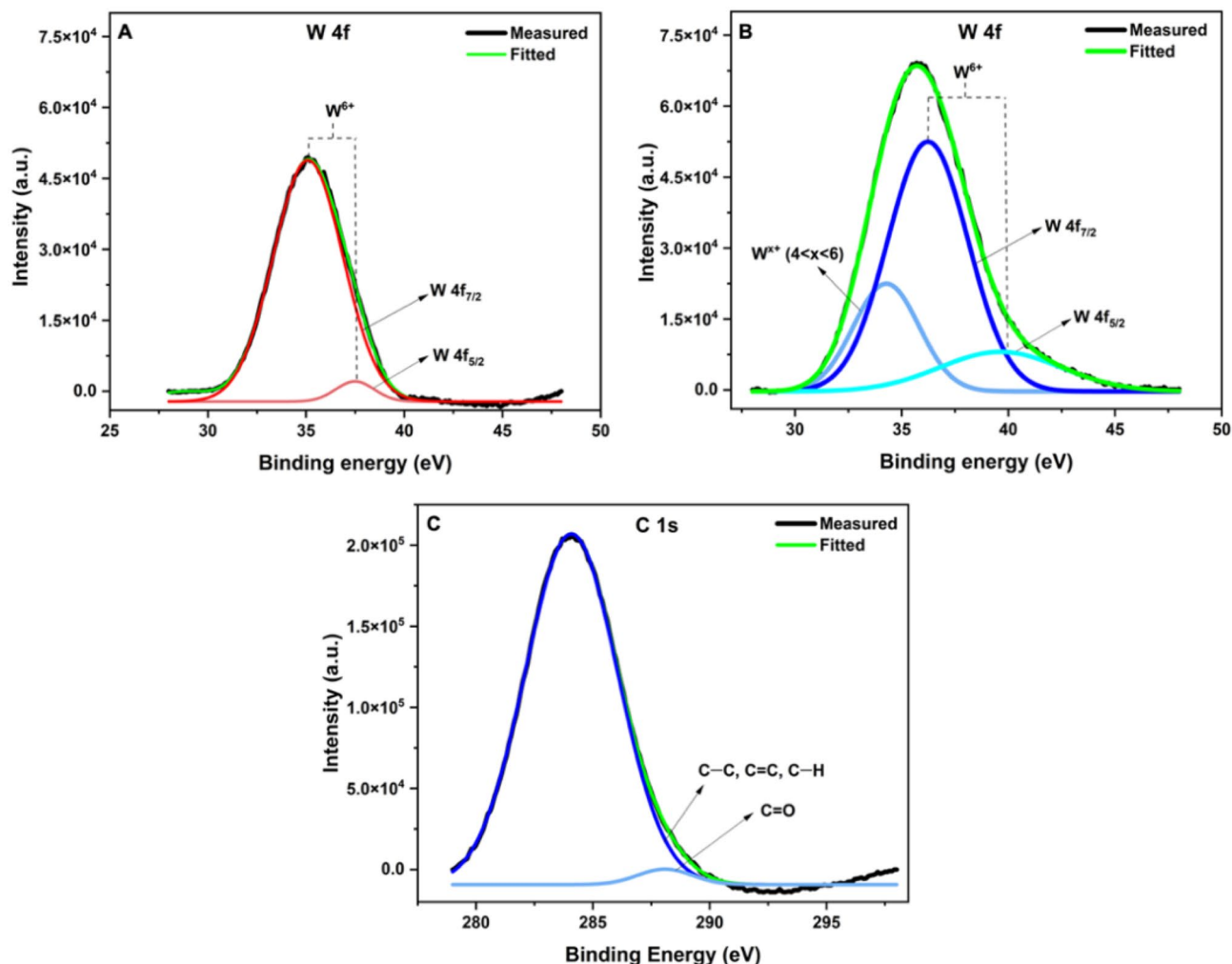
Figure 4. XPS spectra of W 4f of (**A**) WO_3 and (**B**) WO_3/C. (**C**) C 1s spectrum of WO_3/C nanocomposite.

samples (Fig. S4). Moreover, the WO_3/C nanocomposite showed a high-intensity C 1s peak, which deconvoluted to two peaks at 284.1 eV and 288.1 eV (Fig. 4C). The former could be ascribed to C–C, C=C, and C–H bonds while the latter to C=O bonds[44]. The presence of these peaks agrees with the FTIR results and further proves the aromatization of carbon during synthesis.

The surface area and pore characteristics were examined by nitrogen adsorption–desorption analysis, as presented in Fig. 5. The isotherm of pure WO_3 closely resembles a type II isotherm, suggesting that it is an aggregation with predominantly macroporous features[45]. The adsorption amount of N_2 for the WO_3/C nanocomposite significantly increased, displaying a type IV isotherm with an apparent hysteresis loop at a relative pressure range of 0.45–0.95, suggesting the presence of abundant mesopores. The presence of such mesopores was further confirmed in the pore size distribution plot, revealing a range of pore radii between 1.5 and 15.0 nm with the highest peak occurring at 2.0 nm. Mesopores (ranging from 2 to 50 nm based on the IUPAC categorization) play a crucial role in enabling the migration of ions towards smaller micropores (those less than 2 nm in size). These facilitate the smooth transportation of ionic substances and the interconnected pore structure supports the formation of an electric double-layer during the charging process [46]. The surface area and pore volume, calculated by the density functional theory (DFT) method, were 4.1 m^2/g and 0.02 cc/g for WO_3 while 58.5 m^2/g and 0.09 cc/g for WO_3/C nanocomposite.

The electrochemical charge storage properties of WO_3 and WO_3/C nanocomposite were evaluated using cyclic voltammetry (CV), galvanostatic charge–discharge (GCD) technique, and impedance spectroscopy. Figure 6A and B display the CV curves of the WO_3 and WO_3/C electrodes between the potential range of − 0.90 to 0.90 V at different scan rates ranging from 20 mV/s to 200 mV/s. The anodic and cathodic currents increased with higher scan rates, which is a normal occurrence in CV. The comparative CV curves (Fig. 7) at a lower scan rate of 20 mV/s show that the WO_3/C electrode maintains a larger area under the CV curve compared to WO_3, indicating better capacitance. Additionally, a control sample containing only carbon particles was also prepared and similarly showed lower capacitance than the nanocomposite (Fig. 7, S2B, S6, S7). Moreover, the quasi-rectangular shape of the CV curve suggests pseudocapacitance. Equation (4) represents the electrochemical charge storage mechanism of WO_3 in the KOH electrolyte[47]:
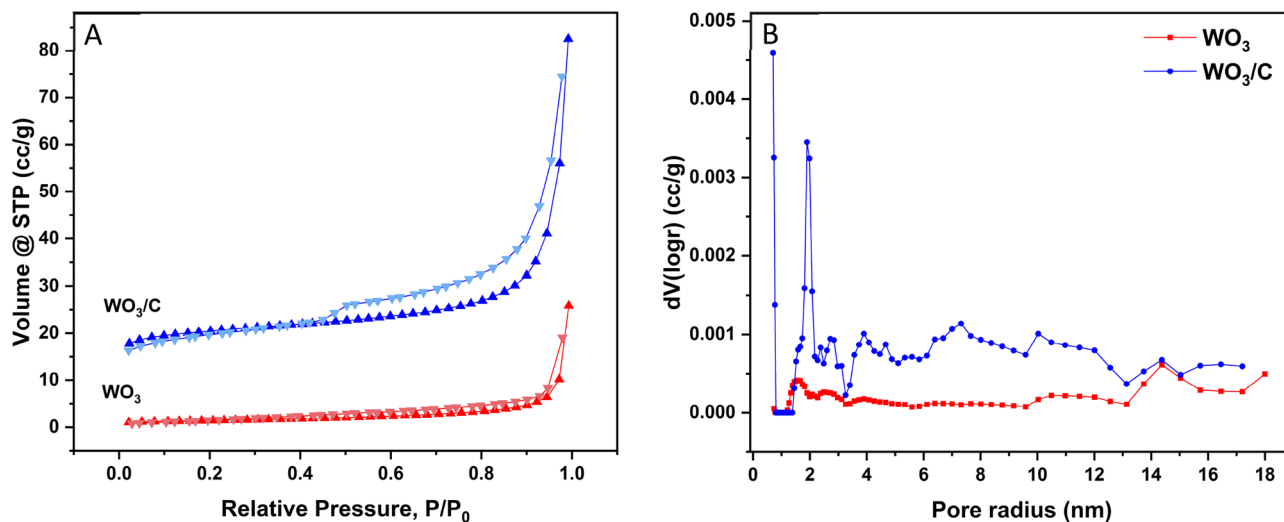
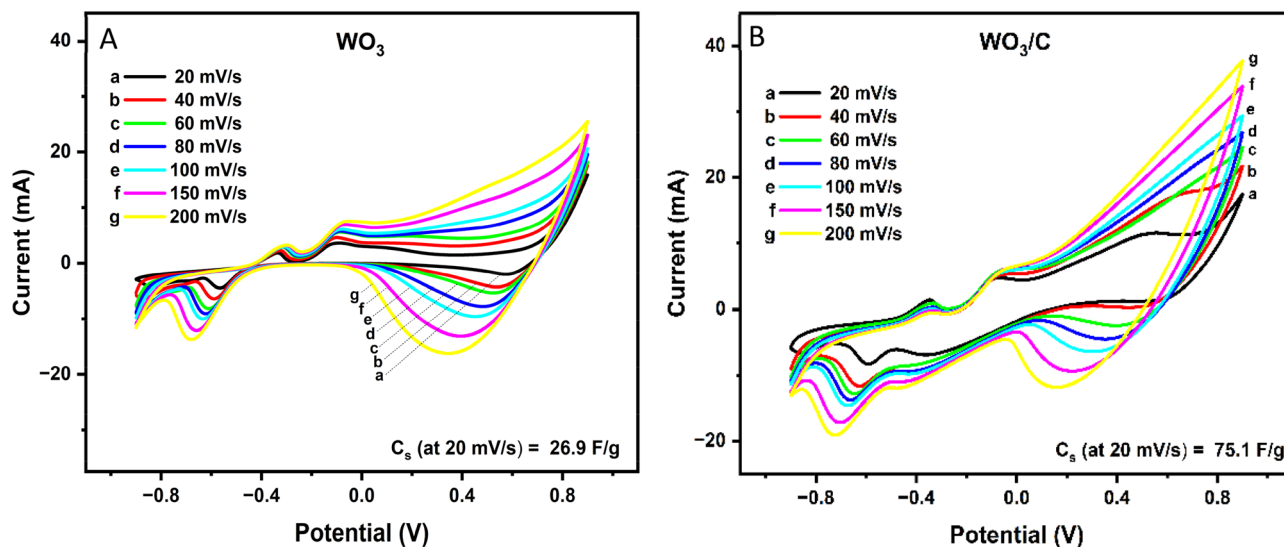**Figure 5.** Nitrogen adsorption–desorption isotherms (**A**) and DFT pore size distribution curves (**B**) of WO_3 and WO_3/C nanocomposite.

Figure 6. Cyclic voltammetry (CV) curves of (**A**) WO_3 and (**B**) WO_3/C nanocomposite at different scan rates.

$$WO_3 + xK^+ + xe^- \leftrightarrow KxWO_3 \tag{4}$$

With background correction from the copper substrate and the carbon control taken into consideration (Fig. 7), the WO_3/C electrode showed an oxidation peak at 0.56 V to 0.76 V (peak E) and a reduction peak at -0.20 V to -0.50 V (peak G). While for the WO_3 electrode, these peaks appeared at 0.0 V to 0.20 V (peak I) and -0.60 V to -0.75 V (peak K). This demonstrated the existence of reversible Faradaic reactions, suggesting an ion intercalation into the crystal structure of the metal oxide[37]. Peaks F and J could not be considered cathodic peaks since this was also present in the carbon control (peak L).

Interestingly, the WO_3/C electrode showed an extra oxidation peak at 0.0 V to -0.05 V (peak H), suggesting an additional irreversible Faradaic reaction. The redox behavior of WO_3 and WO_3/C aligned with the W 4f. XPS results, revealing two oxidation states for WO_3/C and only one for WO_3. The two oxidation peaks of the nanocomposite could be assigned to the electroactivity of W^{6+} and W^{x+} ($4 < x < 6$). It was also observed that the redox peaks became less pronounced at higher scan rates (Fig. 6), which is due to the rapid charge kinetics caused by the high electric field[37].

Using Eq. (1), the specific capacitance of the WO_3 and WO_3/C electrodes was calculated from the CV data. As shown in Fig. S7, the specific capacitance exponentially increased with decreasing scan rate. At a high scan rate of 200 mV/s, there was only a small difference between the specific capacitance of WO_3 and WO_3/C electrodes (14.4 F/g and 16.2 F/g). However, as the scan rate decreased, the difference became more apparent. At 20 mV/s, the specific capacitance of WO_3/C increased to 75.1 F/g while WO_3 increased to only 26.8 F/g. The values are
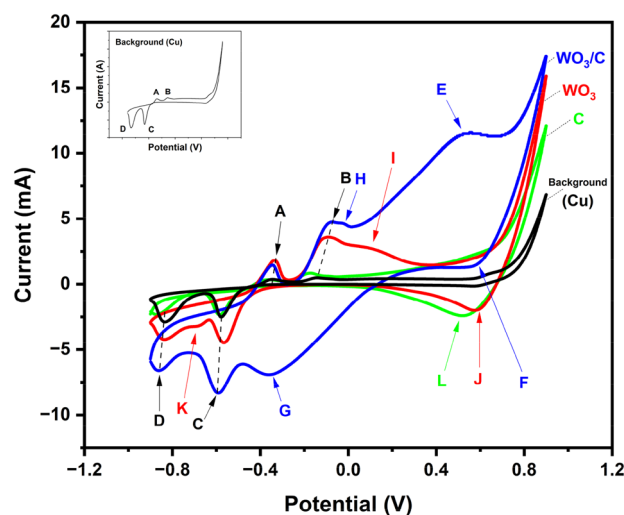
Figure 7. Comparative CV curves at 20 mV/s scan rate of WO₃/C, WO₃, C, and background signal from the Cu substrate.

comparable to that of reported in the literature (Supporting Information Table 1). The observed increase in capacitance at lower scan rates aligns with the typical rate performance in energy storage devices. Lower scan rates allow better diffusion of electrolyte ions to reach the cavities within the electrode material's internal structure while at higher scan rates, ions may get only surface immersion[47,48]. Overall, the higher capacitance of the WO₃/C nanocomposite affirmed that it has more pathways for charge diffusion within its structure. These pathways were most likely a synergistic effect of the complex mixed-phase (tetragonal/monoclinic) WO₃ forming a hierarchical structure with the mesoporous carbon microspheres, resulting in an expanded surface area. Both the presence of mesopores, which decrease ion transport resistance, and the Faradaic reactions significantly enhance electrochemical performance throughout the charging and discharging process[49].

Figure 8 shows the GCD curves of the electrodes and their cycling stability. The deviation from the typical triangular shape further supported the pseudocapacitive behavior of the electrode materials. Using Eq. (2), WO₃/C showed a higher coulombic efficiency than WO₃. The former exhibited 98.2% efficiency at a current density of 1 A/g while the latter showed 75.8% at the same current density. The nanocomposite material also showed higher energy efficiency (92.8% at 1 A/g) than the pure WO₃ (65.1%). Additionally, the cycling stability test demonstrated that the WO₃ and WO₃/C electrodes retained 68.5% and 83.2% of their capacitance, respectively, after 800 GCD cycles. This enhanced capacity retention in the nanocomposite affirmed that the inclusion of carbon contributes to the material's structural stability. Notably, the particle morphology of WO₃/C remained unchanged after cycling, as depicted in Figure S8. However, the decrease in the performance for both electrodes could be explained by the possible distortion of the crystal lattice of tungsten oxide which could have adversely affected the charge transport [40].

The charge transfer ability and interface resistance of the WO₃ and WO₃/C electrodes were studied by electrochemical impedance spectroscopy (EIS). Figure 9 shows the Nyquist plot of EIS measurements performed from 1 Hz to 100 kHz. The semicircular arc in the high-frequency region is indicative of the charge-transfer resistance (R_{ct}) attributed to Faradaic reactions at the electrode/electrolyte interface[6,50]. WO₃/C showed a lower resistance at $R_{ct} = 11.7\Omega$ compared to WO₃ at $R_{ct} = 14.0\Omega$. The arc could also be attributed to bulk electrolyte resistance (R_∞) while the distance from the imaginary impedance axis ($-Z''$), to the electrode resistance (R_e). The sum of
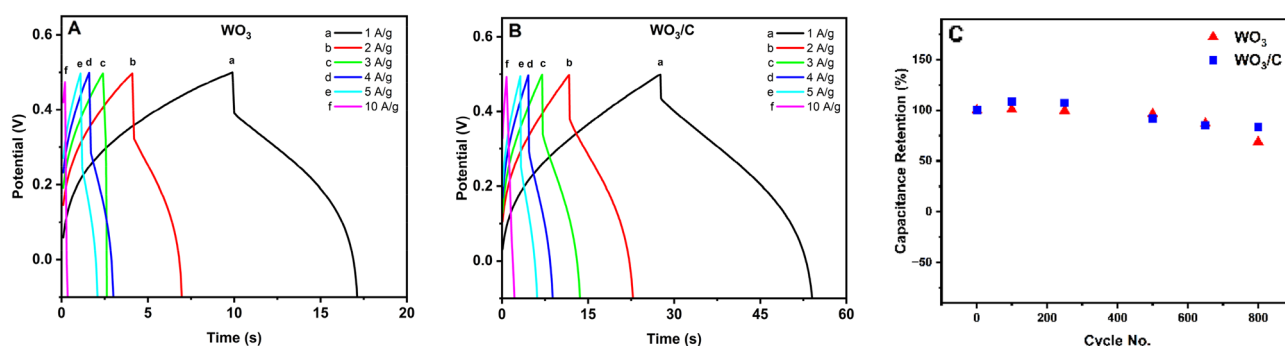

Figure 8. Galvanostatic charge–discharge (GCD) curves for (**A**) WO₃ and (**B**) WO₃/C electrodes. (**C**) GCD cycling stability.
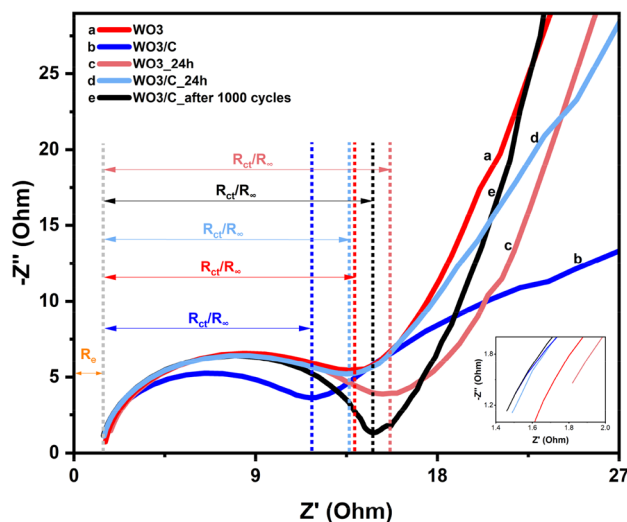
Figure 9. Nyquist plot of the electrochemical impedance. Inset: Emphasis on the difference.

these two accounts for the total internal resistance of the electrode[51]. The inset in Fig. 9 shows that WO_3/C also demonstrated a lower R_e than WO_3. The conductivity was found to be 0.55 S/m for WO_3 and 0.68 S/m for WO_3/C. A sloped line related to Warburg resistance or diffuse layer resistance was present at the low-frequency region. From a physical interpretation of this line, steep slopes indicate that the dominating process is electric double-layer (EDL) formation, while it is ion diffusion at low slopes[51]. Interestingly, the WO_3/C electrode showed a low slope (b in blue), but after 24 h of stabilization in the electrolyte the slope became steeper (d in light blue). But for WO_3, the slope was already steep (a in red) and did not change much after 24 h (c in light red). This observation supports more channels in the nanocomposite arising from both the inner crystal structure and the amorphous carbon network. The relatively deep insertion of ions leads to a relatively longer time for the EDL to form, and thus ion diffusion was still the dominating process at the beginning[40]. After 24 h, the R_{ct} for WO_3/C and WO_3 were 13.6Ω and 15.7Ω, respectively. Moreover, for WO_3/C, the EIS spectra after 1000 CV cycles showed an R_{ct} of 14.9Ω and the steepest slope, suggesting effective ion physisorption at the electrode/electrolyte interface.

Conclusion

A facile hydrothermal method successfully prepared a hierarchical nano/microstructure WO_3/C nanocomposite. Glucose, used as the carbon-source precursor, also influenced the crystal phase transformation of WO_3. It contained a phase junction of tetragonal/monoclinic WO_3 uniformly embedded on carbon microspheres and exhibited more oxidation states. Owing to this distinctive structure, the WO_3/C electrode exhibited better electrochemical performance with a specific capacitance of 75.1 F/g compared to pure WO_3 with 26.8 F/g at a scan rate of 20 mV/s in 0.1 M KOH. A pseudocapacitive behavior was observed, with WO_3/C showing a high coulombic efficiency at 98.2% at a current density of 1 A/g. Cyclic voltammetry and impedance spectroscopy results suggested that the nanocomposite's energy storage mechanism showed both Faradaic and non-Faradaic capacitance.

Data availability

The data generated or analyzed during this study are available within the article and its supplementary material. Raw data of XRD, FTIR, Raman, SEM, TEM, XPS, electrochemical impedance, cyclic voltammetry, and galvanostatic charge–discharge are provided in the supplementary material (Raw data). All other data is available from the corresponding author upon request.

References

1. Purkait, T., Singh, G., Kumar, D., Singh, M. & Dey, R. S. High-performance flexible supercapacitors based on electrochemically tailored three-dimensional reduced graphene oxide networks. *Sci. Rep.* https://doi.org/10.1038/s41598-017-18593-3 (2018).
2. Niu, Q., Gao, K. & Shao, Z. Cellulose nanofiber/single-walled carbon nanotube hybrid non-woven macrofiber mats as novel wearable supercapacitors with excellent stability, tailorability and reliability. *Nanoscale* **6**(8), 4083–4088. https://doi.org/10.1039/c3nr05929d (2014).
3. Wang, C., Xiong, Y., Wang, H. & Sun, Q. All-round utilization of biomass derived all-solid-state asymmetric carbon-based supercapacitor. *J. Colloid Interface Sci.* **528**, 349–359. https://doi.org/10.1016/j.jcis.2018.05.103 (2018).
4. Ye, M. *et al.* ZnFe$_2$O$_4$/graphitic carbon nitride nano/microcomposites for the enhanced electrochemical sensing of H$_2$O$_2$. *ACS Appl.. Nano Mater.* https://doi.org/10.1021/acsanm.2c02204 (2022).
5. Shinde, P. A. & Jun, S. C. Review on recent progress in the development of tungsten oxide based electrodes for electrochemical energy storage. *ChemSusChem* **13**(1), 11–38. https://doi.org/10.1002/cssc.201902071 (2020).
6. Shao, Z. *et al.* Hierarchical micro/nanostructured WO$_3$ with structural water for high-performance pseudocapacitors. *J. Alloys Compd.* **765**, 489–496. https://doi.org/10.1016/j.jallcom.2018.06.192 (2018).

7. Liu, X., Sheng, G., Zhong, M. & Zhou, X. Dispersed and size-selected WO$_3$ nanoparticles in carbon aerogel for supercapacitor applications. *Mater. Des.* **141**, 220–229. https://doi.org/10.1016/j.matdes.2017.12.038 (2018).
8. Bastakoti, B. P., Huan, H. S., Chen, L. C. & Yamauchi, Y. Block copolymer assisted synthesis of porous α-Ni(OH)$_2$ microflowers with high surface areas as electrochemical pseudocapacitor materials. *Chem. Commun.* **48**(73), 9150–9152. https://doi.org/10.1039/c2cc32945j (2012).
9. Mineo, G., Bruno, E. & Mirabella, S. Advances in WO$_3$-based supercapacitors: State-of-the-art research and future perspectives. *Nanomaterials* https://doi.org/10.3390/nano13081418 (2023).
10. Bentley, J. & Bastakoti, B. P. Block copolymer templated synthesis of mesoporous WO$_3$/carbon nanocomposites. *J. Mater. Sci.* **57**(31), 14772–14779. https://doi.org/10.1007/s10853-022-07564-3 (2022).
11. Ou, P. *et al.* WO$_3$·nH$_2$O crystals with controllable morphology/phase and their optical absorption properties. *ACS Omega* **7**(10), 8833–8839. https://doi.org/10.1021/acsomega.1c07147 (2022).
12. Bentley, J., Desai, S. & Bastakoti, B. P. Porous tungsten oxide: Recent advances in design, synthesis, and applications. *Chem. Eur. J.* **27**(36), 9241–9252. https://doi.org/10.1002/chem.202100649 (2021).
13. Yang, H. *et al.* Structural, electronic, optical and lattice dynamic properties of the different WO$_3$ phases: First-principle calculation. *Vacuum* **164**, 411–420. https://doi.org/10.1016/j.vacuum.2019.03.053 (2019).
14. Liu, X., Tan, J., Li, X. & Zhang, C. Glucose-assisted one-pot hydrothermal synthesis of hierarchical-structured mos2/c quasi-hollow microspheres for high-performance lithium ion battery. *Polymers (Basel)* **13**(5), 1–12. https://doi.org/10.3390/polym13050837 (2021).
15. Guillén-López, A. *et al.* The influence of tungsten oxide concentration on a carbon surface for capacitance improvement in energy storage devices: A combined experimental and theoretical study. *J. Phys. Chem. Solids* https://doi.org/10.1016/j.jpcs.2022.110610 (2022).
16. Bastakoti, B. P. *et al.* Polymeric micelle assembly for preparation of large-sized mesoporous metal oxides with various compositions. *Langmuir* **30**(2), 651–659. https://doi.org/10.1021/la403901x (2014).
17. Nayak, A. K., Das, A. K. & Pradhan, D. High performance solid-state asymmetric supercapacitor using green synthesized graphene-WO$_3$ nanowires nanocomposite. *ACS Sustain. Chem. Eng.* **5**(11), 10128–10138. https://doi.org/10.1021/acssuschemeng.7b02135 (2017).
18. Xiong, Y., Wang, C., Jin, C., Sun, Q. & Xu, M. discarded biomass derived ordered hierarchical porous WO$_3$-C as advanced electrochemical materials. *ACS Sustain. Chem. Eng.* **6**(11), 13897–13906. https://doi.org/10.1021/acssuschemeng.8b02138 (2018).
19. Shi, F. *et al.* Three-dimensional hierarchical porous lignin-derived carbon/WO$_3$ for high-performance solid-state planar micro-supercapacitor. *Int. J. Biol. Macromol.* **190**, 11–18. https://doi.org/10.1016/j.ijbiomac.2021.08.183 (2021).
20. Di, J., Xu, H., Gai, X., Yang, R. & Zheng, H. One-step solvothermal synthesis of feather duster-like CNT@WO$_3$ as high-performance electrode for supercapacitor. *Mater. Lett.* **246**, 129–132. https://doi.org/10.1016/j.matlet.2019.03.070 (2019).
21. Isacfranklin, M. *et al.* Marigold flower like structured Cu$_2$NiSnS$_4$ electrode for high energy asymmetric solid state supercapacitors. *Sci. Rep.* https://doi.org/10.1038/s41598-020-75879-9 (2020).
22. Sun, X. & Li, Y. Colloidal carbon spheres and their core/shell structures with noble-metal nanoparticles. *Angewandte Chem. Int. Edition* **43**(5), 597–601. https://doi.org/10.1002/anie.200352386 (2004).
23. Ibukun, O. & Jeong, H. K. An activated carbon and carbon nanotube composite for a high-performance capacitor. *New Phys. Sae Mulli* **68**(2), 185–188. https://doi.org/10.3938/NPSM.68.185 (2018).
24. Laheäär, A., Przygocki, P., Abbas, Q. & Béguin, F. Appropriate methods for evaluating the efficiency and capacitive behavior of different types of supercapacitors. *Electrochem. Commun.* **60**, 21–25. https://doi.org/10.1016/j.elecom.2015.07.022 (2015).
25. Ke, J. *et al.* Crystal transformation of 2D tungstic acid H$_2$WO$_4$ to WO$_3$ for enhanced photocatalytic water oxidation. *J. Colloid Interface Sci.* **514**, 576–583. https://doi.org/10.1016/j.jcis.2017.12.066 (2018).
26. Chen, D., Gao, L., Yasumori, A., Kuroda, K. & Sugahara, Y. Size- And shape-controlled conversion of tungstate-based inorganic-organic hybrid belts to WO$_3$ nanoplates with high specific surface areas. *Small* **4**(10), 1813–1822. https://doi.org/10.1002/smll.200800205 (2008).
27. Cao, J., Luo, B., Lin, H., Xu, B. & Chen, S. Thermodecomposition synthesis of WO$_3$/H$_2$WO$_4$ heterostructures with enhanced visible light photocatalytic properties. *Appl. Catal. B* **111–112**, 288–296. https://doi.org/10.1016/j.apcatb.2011.10.010 (2012).
28. Hariharan, V., Radhakrishnan, S., Parthibavarman, M., Dhilipkumar, R. & Sekar, C. Synthesis of polyethylene glycol (PEG) assisted tungsten oxide (WO$_3$) nanoparticles for l-dopa bio-sensing applications. *Talanta* **85**(4), 2166–2174. https://doi.org/10.1016/j.talanta.2011.07.063 (2011).
29. Liu, F., Chen, X., Xia, Q., Tian, L. & Chen, X. Ultrathin tungsten oxide nanowires: Oleylamine assisted nonhydrolytic growth, oxygen vacancies and good photocatalytic properties. *RSC Adv.* **5**(94), 77423–77428. https://doi.org/10.1039/c5ra12993a (2015).
30. Ponnusamy, R., Chakraborty, B. & Rout, C. S. Pd-doped WO$_3$ nanostructures as potential glucose sensor with insight from electronic structure simulations. *J. Phys. Chem. B* **122**(10), 2737–2746. https://doi.org/10.1021/acs.jpcb.7b11642 (2018).
31. Kang, M. *et al.* Structural design of hexagonal/monoclinic WO3 phase junction for photocatalytic degradation. *Mater. Res. Bull.* https://doi.org/10.1016/j.materresbull.2019.110614 (2020).
32. Khudadad, A. I., Yousif, A. A. & Abed, H. R. Effect of heat treatment on WO$_3$ nanostructures based NO$_2$ gas sensor low-cost device. *Mater. Chem. Phys.* https://doi.org/10.1016/j.matchemphys.2021.124731 (2021).
33. Usta, M., Kahraman, S., Bayansal, F. & Çetinkara, H. A. Effects of annealing on morphological, structural and electrical properties of thermally evaporated WO$_3$ thin films. *Superlattices Microstruct.* **52**(2), 326–335. https://doi.org/10.1016/j.spmi.2012.05.008 (2012).
34. Thummavichai, K. *et al.* In situ investigations of the phase change behaviour of tungsten oxide nanostructures. *R. Soc. Open Sci.* https://doi.org/10.1098/rsos.171932 (2018).
35. Kumar, N., Haviar, S., Rezek, J., Baroch, P. & Zeman, P. Tuning stoichiometry and structure of Pd-WO$_{3-x}$ thin films for hydrogen gas sensing by high-power impulse magnetron sputtering. *Materials* **13**(22), 1–12. https://doi.org/10.3390/ma13225101 (2020).
36. Lokhande, V., Lokhande, A., Namkoong, G., Kim, J. H. & Ji, T. Charge storage in WO$_3$ polymorphs and their application as supercapacitor electrode material. *Results Phys.* **12**, 2012–2020. https://doi.org/10.1016/j.rinp.2019.02.012 (2019).
37. Gupta, S. P. *et al.* Phase transformation in tungsten oxide nanoplates as a function of post-annealing temperature and its electrochemical influence on energy storage. *Nanoscale Adv.* **2**(10), 4689–4701. https://doi.org/10.1039/d0na00423e (2020).
38. Li, X. *et al.* Efficient solar-driven nitrogen fixation over carbon–tungstic-acid hybrids. *Chem. A Eur. J.* **22**(39), 13819–13822. https://doi.org/10.1002/chem.201603277 (2016).
39. Wei, C., Jin, X., Wu, C., Brozovic, A. & Zhang, W. Carbon spheres with high photothermal conversion efficiency for photothermal therapy of tumor. *Diam. Relat. Mater.* https://doi.org/10.1016/j.diamond.2022.109048 (2022).
40. Liu, X. D. *et al.* Oxygen vacancy-rich WO$_3$ heterophase structure: A trade-off between surface-limited pseudocapacitance and intercalation-limited behaviour. *Chem. Eng. J.* https://doi.org/10.1016/j.cej.2021.131431 (2021).
41. Sun, W., Li, C., Bai, J. & Xing, L. Carbon nanofibers-assembled tungsten oxide as unique hybrid electrode materials for high-performance symmetric supercapacitors. *Energy Fuels* **35**(14), 11572–11579. https://doi.org/10.1021/acs.energyfuels.1c01428 (2021).
42. Basic Quantification of XPS Spectra, 2008. [Online]. Available: www.casaxps.com
43. Yu, B. & Chen, Y. Conductive WO$_3$-x@CNT networks for efficient Li-S batteries. *IOP Conf. Ser. Mater. Sci. Eng.* https://doi.org/10.1088/1757-899X/892/1/012027 (2020).

44. Belardja, M. S., Djelad, H., Lafjah, M., Chouli, F. & Benyoucef, A. The influence of the addition of tungsten trioxide nanoparticle size on structure, thermal, and electroactivity properties of hybrid material-reinforced PANI. *Colloid Polym. Sci.* https://doi.org/10.1007/s00396-020-04720-6/Published (2020).

45. Zhang, Q., Zhang, Y., Chen, J. & Liu, Q. Hierarchical structure kaolinite nanospheres with remarkably enhanced adsorption properties for methylene blue. *Nanoscale Res. Lett.* https://doi.org/10.1186/s11671-019-2934-x (2019).

46. Supiyeva, Z., Pan, X. & Abbas, Q. The critical role of nanostructured carbon pores in supercapacitors. *Curr. Opin. Electrochem.* https://doi.org/10.1016/j.coelec.2023.101249 (2023).

47. Mohan, V. V., Anjana, P. M. & Rakhi, R. B. A study on the effect of phase conversion of tungsten nanostructures on their electrochemical energy storage performance. *Mater. Adv.* **3**(14), 5900–5910. https://doi.org/10.1039/d2ma00475e (2022).

48. Sun, K. *et al.* An asymmetric supercapacitor based on controllable WO_3 nanorod bundle and alfalfa-derived porous carbon. *RSC Adv.* **11**(59), 37631–37642. https://doi.org/10.1039/d1ra04788d (2021).

49. Qu, X. *et al.* Effect of different pretreatment methods on sesame husk-based activated carbon for supercapacitors with aqueous and organic electrolytes. *J. Mater. Sci. Mater. Electron.* https://doi.org/10.1007/s10854-019-01107-4 (2019).

50. Lin, J. & Du, X. High performance asymmetric supercapacitor based on hierarchical carbon cloth in situ deposited with h-WO_3 nanobelts as negative electrode and carbon nanotubes as positive electrode. *Micromachines (Basel)* https://doi.org/10.3390/mi12101195 (2021).

51. Mei, B. A., Munteshari, O., Lau, J., Dunn, B. & Pilon, L. Physical interpretations of nyquist plots for EDLC electrodes and devices. *J. Phys. Chem. C* **122**(1), 194–206. https://doi.org/10.1021/acs.jpcc.7b10582 (2018).

Acknowledgements

Author contributions

B.P.B. designed the project and supervised. S.M.M.A. and J.B. did experiment. S.M.M.A. prepared the first draft. B.P.B. and S.M.M.A., J.B. and S.D. revised the manuscript.

Competing interests

The authors declare no competing interests.

Additional information

Supplementary Information The online version contains supplementary material available at https://doi.org/10.1038/s41598-023-48958-w.

Correspondence and requests for materials should be addressed to B.P.B.

Reprints and permissions information is available at www.nature.com/reprints.

Publisher's note Springer Nature remains neutral with regard to jurisdictional claims in published maps and institutional affiliations.